EPJ Web of Conferences **153**, 04002 (2017) DOI: 10.1051/epjconf/201715304002
ICRS-13 & RPSD-2016

Double differential neutron yields from thick targets used in space applications

Natalie A. McGirl[1,*], *Luis* A. Castellanos[1], *Ashwin* P. Srikrishna[1], *Lawrence* H. Heilbronn[1], *Chiara* La Tessa[2], *Adam* Rusek[2], *Michael* Sivertz[2], *Steve* Blattnig[3], *Martha* Clowdsley[3], *Tony* Slaba[3], and *Cary* Zeitlin[4]

[1]Department of Nuclear Engineering, University of Tennessee, 1004 Estabrook Rd, Knoxville, TN, USA, 37996
[2]NASA Space Radiation Laboratory, Brookhaven National Laboratory, Upton, NY, USA, 11973
[3]NASA, Langley Research Center, Hampton, VA, USA, 23681
[4]Lockheed Martin, Information Systems and Global Solutions, Houston, TX, USA, 77285

Abstract. In March 2016, secondary neutron production from thick-target shielding experiments were conducted at the National Aeronautics and Space Administration's (NASA) Space Radiation Laboratory at Brookhaven National Laboratory. Ion beams of proton, helium, and iron projectiles were aimed at aluminum targets with areal densities of 20, 40, and 60 g/cm^2. The ion beams were extracted at energies of 400 and 800 AMeV and neutron yields were measured with liquid scintillators at 10°, 30°, 45°, 60°, 80°, and 135° off the beam axis. A second 60 g/cm^2 aluminum target was placed 3.5 m downstream from the middle of front target to study backscattered neutrons. Double differential thick-target neutron yields for various combinations of projectile, projectile energy, target material, target thickness, and detector location were produced using the time-of-flight technique. These measurements will help NASA perform uncertainty analyses on their transport codes and contribute to shielding design studies for future space applications.

1 Introduction

The future of manned, deep-space missions includes the need to sufficiently protect astronauts from the ionizing radiation effects caused by Solar Energetic Particles (SEP) and Galactic Cosmic Rays (GCR) for an extended length of time. Habitats and other transit vehicles often contain areas of thick (30-40 g/cm^2 or greater) shielding materials such as aluminum or high density polyethylene (HDPE) [1]. While an enclosed, thickly-shielded environment may decrease an astronaut's exposure to the primary radiation field, the creation of a secondary radiation field, which includes neutrons and light charged ions, still poses a risk [2]. In particular, secondary neutrons are a concern due to their highly-penetrative nature and large dose equivalent conversion factors [3]. The purpose of this study is to determine the double differential thick-target yields for neutrons produced directly from GCR-like heavy ion interactions with aluminum or HDPE shielding. These results will be compared with transport model calculations and incorporated into the uncertainty analysis for transport codes developed by the National Aeronautics and Space Administration (NASA). This paper presents a selection of results from an experiment conducted in March 2016.

2 Experiment Overview

Secondary neutron production measurements for the 100-hour March 2016 experiment occurred at Brookhaven National Laboratory's (BNL) NASA Space Radiation Laboratory (NSRL). BNL's Booster accelerator was used to deliver the 400- and 800-MeV protons, 400-AMeV helium, and the 400 and 800-AMeV iron beams to the 20, 40, and 60 g/cm^2 thick aluminum targets (100 x 30 cm^2). A back aluminum target with an areal density of 60 g/cm^2 (100 x 100 x 22.2 cm^3) was placed 3.5 m downstream from the middle of the front target. The addition of this target allowed for the study of neutrons scattered from or produced in the back target, which will occur at a later date. Additionally, two beam-defining EJ-228 plastic scintillator detectors were placed directly in front of the forward target and identified valid beam particles from coincidence events.

Neutrons were detected with three EJ-301 liquid scintillators placed at 10°, 30°, 45°, and three EJ-309 liquid scintillators placed at 60°, 80°, and 135° off the beam axis, with flight paths ranging from 2 to 3 m from the center of the front target to the front face of the liquid scintillator. Each liquid scintillator was 12.7 cm in diameter and 12.7 cm tall. Two thin EJ-304 solid plastic scintillators (12.7 x 12.7 x 0.635 cm^3) covered the front face of each liquid scintillator to distinguish between incident neutral and charged particle events. Finally, a shadow bar system was used to allow for full background characterization. This system consisted of two iron bars with lengths of 1 and 2 m. These shadow bars fully blocked the front face of a liquid scintillator and prevented neutrons originating directly from the front target from entering the scintillator. Liquid scintillator

* Corresponding author: nmcgirl@vols.utk.edu

locations, target locations, and flight path values are shown in Figure 1.

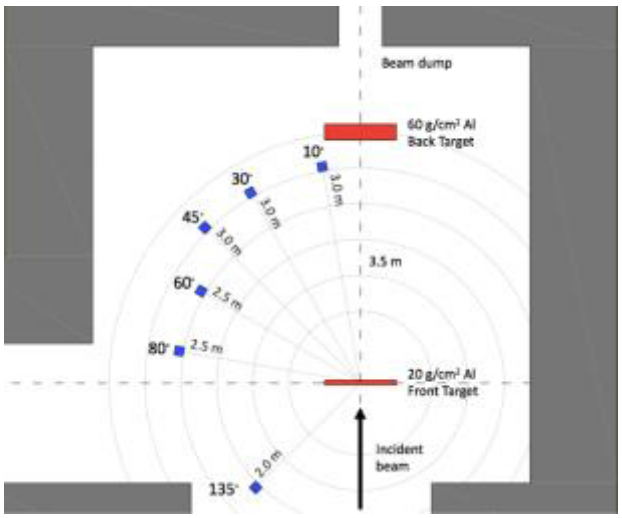

Fig. 1. March 2016 NSRL target room experimental setup for 20 g/cm^2 front and 60 g/cm^2 back aluminum targets. Grey blocks represent concrete walls.

3 Neutron Time of Flight Analysis

Several steps were taken to determine the double differential thick-target neutron yields for the March 2016 100-hour experiment. First, the charge deposited in the beam-defining "start" scintillators were plotted against each other. A noticeable beam spot was identified and a graphical ROOT cut was taken around it [4]. This ensured that only beam particles that did not deviate too far from the center of the beam were taken as source particles incident upon the front target. On average, approximately 30% of the beam particles were eliminated from the analysis with the good beam cut.

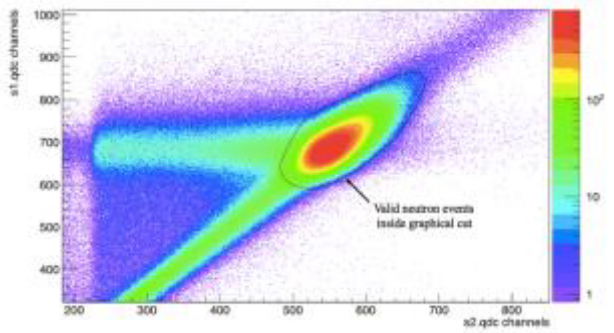

Fig. 2. Charge deposited in start scintillators for a 400-AMeV iron beam with good beam cut boundaries displayed.

Next, the neutral and charged particle events that set the liquid scintillator trigger were gated on in ROOT by selecting the self-time peak in the time-to-digital conversion (TDC) spectrum. The contributions to the liquid scintillator signals were then separated using the thin EJ-304 "veto" detectors located in front of the scintillators. Events that registered in both the veto and liquid scintillator detectors were taken to be the result of a charged particle interaction, due to the low probability of a neutron or gamma interaction in the veto detector [5].

By examining the veto detector's charge-to-digital converter (QDC) output, the neutral and charged particle information was separated and the neutral particle data were refined further to determine the neutron and gamma signal contributions.

Pulse shape discrimination (PSD) was used to separate neutrons and gammas based on the differences between the charge contained in the first 20 to 35 ns of a signal (h_qdc) and in the total signal (t_qdc) [6]. An example of a typical PSD plot is shown in Figure 3. The lowest energy of neutron-gamma separation was examined by taking one-channel-wide slices of the PSD plots and projecting them onto the Y-axis. The resulting neutron and gamma peaks were considered well-separated if their 2σ values did not overlap. The channel number at the separation threshold was converted to incident neutron energy (MeV) using the experimentally determined calibration curves of the liquid scintillators and a light output calibration [7]. Because a neutron may deposit all of its energy in a single interaction, the energy at the separation threshold represented the lowest energy neutron detectable by the scintillator. A 4.0 MeV neutron was detected at the separation threshold for the scintillators at 10°, 30°, and 45°, while a 2.0 MeV neutron was detected at the separation threshold for the scintillators at 60°, 80°, and 135°. Afterwards, neutron and gamma event data were extracted from the PSD plots using ROOT graphical cuts.

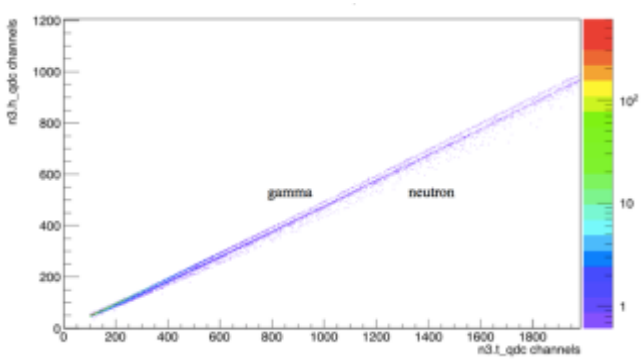

Fig. 3. Neutron and gamma PSD at 45° for 400-MeV protons on 20, 40, and 60 g/cm^2 aluminum front targets; 60 g/cm^2 back aluminum target.

To convert the start scintillator's time-to-digital converter (TDC) outputs to neutron energy spectra, the time-of-flight (TOF) method was utilized. TDC spectra collection started with a coincidence between the beam-defining scintillators and a neutron detector, and stopped once a delayed signal from the beam-defining scintillators was registered. To determine the neutron times of flight, a reference channel number, which corresponded to the gammas that were created in the projectile-target interactions and subsequently detected in the liquid scintillators, was identified on the TDC spectra. This channel number was found by plotting the TDC spectra gated on the gammas identified in PSD. The centroid of the resulting prompt gamma peak was used as the reference channel number, which was different for each beam-target combination.

Before the neutron TOF could be calculated, the background neutron contributions were taken into consideration. During the experiment, multiple runs were taken for each beam-target configuration with and without a shadow bar covering the front face of the liquid scintillators. Because runs varied in duration, system live time, and source particle exposure, counts ($N_{measured}$) in each covered run were combined and normalized to the recorded number of source particles ($s_1 \cdot s_2$), good beam fraction (GB), and live time (LT) per equation 1. This process was then repeated for the uncovered runs. After normalization, the sum of the covered runs for a given beam-target combination were subtracted from the sum of the uncovered runs. This meant the final spectra only contained information for neutrons coming directly from the front target, and not background neutrons that entered from the sides of the liquid scintillator or background neutrons that bypassed the shadow bars by skipping off the floor and entered the front of the scintillator.

$$Yield = \frac{\sum_{i=1}^{n} \frac{N_{i(measured)}}{LT_i}}{\sum_{i=1}^{n} GB_i \times (s_1 \cdot s_2)_i} \quad (1)$$

Neutron times of flight (t_n), velocities ($\beta_n = v_n / c$), and kinetic energies (T_n) were calculated using equations 2 through 5, respectively. The TDC calibration (k) varied from 0.228 ns/channel to 0.238 ns/channel, depending upon the liquid scintillator. Neutron flight paths (d) also varied depending upon the liquid scintillator. The prompt gamma peak channel number (tdc_g) was dependent upon the beam-target combination, while gamma velocity (c) and the neutron rest mass (m_n) were constant values. Finally, the TDC channel number of neutron events (tdc_n) were taken from the TDC output spectra.

$$t_n = (d / c) + k\,(tdc_g - tdc_n) \quad (2)$$

$$v_n = d / t_n \quad (3)$$

$$T_n = (\gamma - 1)\, m_n \quad (4)$$

$$\gamma = (1 - \beta_n^2)^{-1} \quad (5)$$

After converting channel number to neutron energy, an energy-dependent neutron detection efficiency correction factor was applied to each bin. Efficiencies were calculated for a 12.7 cm in length, 12.7 cm in diameter cylindrical liquid scintillator placed 2.0, 2.5, and 3.0 m away from a neutron source using the SCINFUL-QMD Monte Carlo code [8]. Double differential thick-target neutron yields were then calculated by dividing the efficiency-adjusted neutron yields by the solid angle of the liquid scintillator and the energy bin width for units of neutrons per source particle per steradian per energy (neutrons / S.P. / Ω / MeV).

Finally, the uncertainties in the counts were taken into consideration. Statistical uncertainties were calculated in ROOT and varied for each bin. Systematic uncertainties included uncertainties in solid angle, neutron detection efficiency, and graphical cuts. Solid angle uncertainties varied from 6.5% to 13.8% depending upon the flight path of the liquid scintillator and the front target thickness. The uncertainty in neutron detection efficiency was estimated at 15% using published experimental and SCINFUL-QMD calculated results [8]. Finally, the uncertainty in the ROOT graphical cuts was estimated at 5%. The summary of these systematic uncertainties organized by front target thickness is included in Table 1.

Table 1. Fractional systematic uncertainties for front aluminum target thicknesses of 20, 40, and 60 g/cm^2.

Type	Fractional Systematic Uncertainties at 10°, 135°		
	20 g/cm^2	**40 g/cm^2**	**60 g/cm^2**
Solid Angle	6.5, 8.7%	8.9, 11.3%	11.4, 13.8%
Detection Efficiency	15%		
ROOT Graphical Cuts	5%		

4 Selection of Experimental Results

A selection of background-subtracted results from the March 2016 experiment are provided below in Figures 4 through 8. Each figure contains double differential thick-target neutron yields at 10° and 135° for a single beam species on the 20, 40, and 60 g/cm^2 front aluminum targets. The 10° yields were multiplied by a factor of 100 to prevent the overlap of the 10° and 135° low-energy yields. Only statistical uncertainties were shown and they varied widely depending upon the ion beam. In general, statistical uncertainties from this experiment decreased with an increase in front target thickness. As the front target thickness increased, the number of nuclear interactions between the incident beam and target material also increased, resulting in a larger production of secondary neutrons. Additionally, an increase in beam energy typically led to lower statistical uncertainties because of the increased number of beam-target interactions. However, this was not seen with the 800-AMeV iron beam, as discussed later. Statistical uncertainties also improved as the neutron energy increased for the 10° liquid scintillator, but the uncertainties worsened at the highest neutron energies (about 60 to 90 MeV) for the 135° liquid scintillator.

Double differential thick-target neutron yields at 10° mostly consisted of neutrons produced during projectile breakup. The characteristic forward angle peak was located at approximately 70% of the incident beam energy and the yields rapidly decreased after this point, as expected. The thick-target neutron measurements and uncertainties at 10° suffered from background subtraction at low energies due to the liquid scintillator's proximity to the back target. Neutrons produced by other secondary ions or reflected off the back target typically had energies less than 100 MeV. These neutrons entered through the sides of the 10° liquid scintillator instead of the front face, which meant they were tagged as background events during the shadowed runs. Additionally, many of the

beams were high enough in energy to punch through the front target, which resulted in secondary neutron production by primary beam interactions in the back target. The higher than expected background yields below 100 MeV resulted in lower-than-expected background-subtracted yields as well as poor statistics from error propagation. While the average fractional uncertainties below 100 MeV varied widely depending upon the ion beam, all average uncertainties above 100 MeV were less than 20%.

Yields at 135° were dominated by low-energy, isotropically emitted neutrons from target evaporation. Detected neutrons at this angle typically had an energy less than 100 MeV and yields exponentially decreased with energy. Statistical uncertainties were best for neutron measurements at 135° when compared to the other liquid scintillator locations due to the low neutron background at back angles. The average fractional uncertainties for all beams at all neutron energies ranged from 3.5% to 10%.

Double differential thick-target neutron yields for the 400-AMeV iron beam are displayed in Figure 4. This beam was stopped in all aluminium target thicknesses, indicating that only secondary particles were emitted from the front target. At 10°, the average fractional statistical uncertainties below 100 MeV for the 20, 40, and 60 g/cm^2 thick beam-target configurations were 12%, 9.5%, and 9.0%, respectively. Above 100 MeV, fractional uncertainties were less than 3.5%.

Figure 5 contains double differential yields for 800-AMeV iron on 20, 40, and 60 g/cm^2 aluminum front targets. Yields generated with the 800-AMeV iron beam were generally higher than with the 400-AMeV iron beam, except with the 20 g/cm^2 beam-target configuration. The 800-AMeV iron beam stopped in the 40 and 60 g/cm^2 aluminum targets, but punched through the 20 g/cm^2 target. This meant that the incident ion beam also interacted in the back 60 g/cm^2 aluminum target, increasing the number of neutrons that entered through the sides of the liquid scintillator at 10°. Double differential yields at 20 g/cm^2 were lower than expected for all secondary neutron energies because of this increase in the "neutron background" close to the back target.

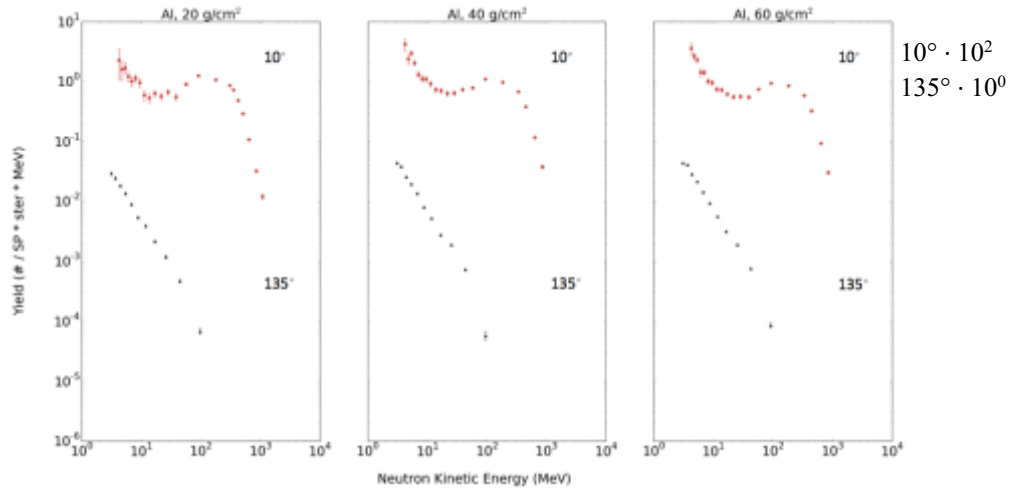

Fig. 4. Background subtracted double differential thick-target neutron yields at 10° and 135° for 400-AMeV iron projectiles on 20, 40, and 60 g/cm^2 front and 60 g/cm^2 back aluminum targets. The 10° yields were multiplied by a factor of 100 to prevent overlap.

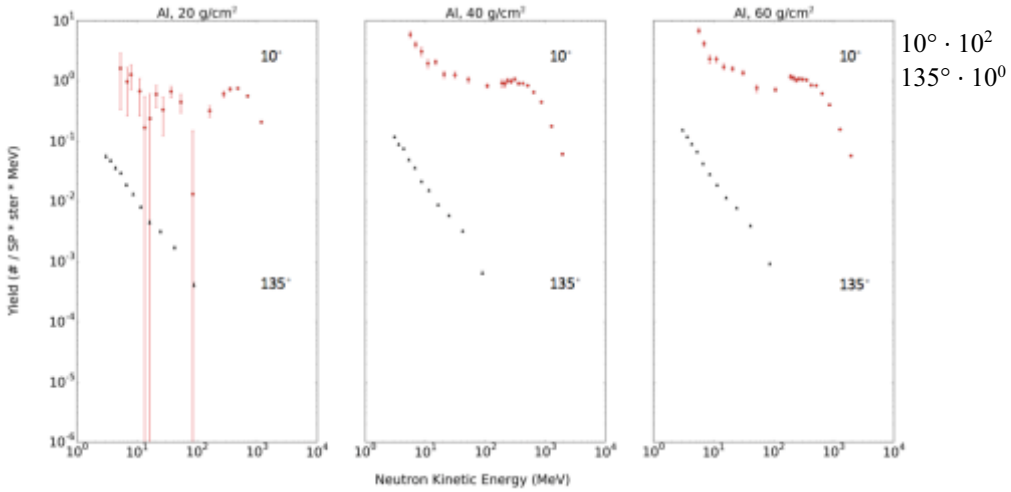

Fig. 5. Background subtracted double differential thick-target neutron yields at 10° and 135° for 800-AMeV iron projectiles on 20, 40, and 60 g/cm^2 front and 60 g/cm^2 back aluminum targets. The 10° yields were multiplied by a factor of 100 to prevent overlap.

Adding the shadowed and unshadowed uncertainties in quadrature resulted in average uncertainties over 100% below 100 MeV. However, the average uncertainty was less than 8.5% above neutron energies of 100 MeV. For the 40 and 60 g/cm^2 target, the average uncertainties below 100 MeV were less than 13%, and less than 5% at higher energies.

Double differential neutron yields for the 400- and 800-MeV proton beams are displayed in Figures 6 and 7. Both beams punched through all front target thicknesses and interacted in the back target, resulting in poor statistics below 100 MeV, similar to what was seen with the 800-AMeV iron beam on 20 g/cm^2 aluminum. Due to the increase in beam-target interactions and subsequent increase in secondary neutrons with a higher beam energy, average uncertainties were lower for the 800-MeV proton system at all target thicknesses when compared with the 400-MeV proton system. Depending upon the target thickness, average uncertainties below 100 MeV for the 400- and 800-MeV proton beams ranged from 32% to 54% and 15% to 31%, respectively. Above 100 MeV, average uncertainties were less than 22% (400-MeV protons) and less than 10% (800-MeV protons).

Finally, the 400-AMeV helium beam-target double differential yields are displayed in Figure 8. While the helium beam also punched through all target thicknesses, the uncertainty issues below 100 MeV were less pronounced than what was seen with the proton beams and the 800-AMeV iron beam on 20 g/cm^2 aluminum. Average uncertainties below 100 MeV ranged from 12% to 27%, depending upon the target thickness, while uncertainties above 100 MeV were less than 5%.

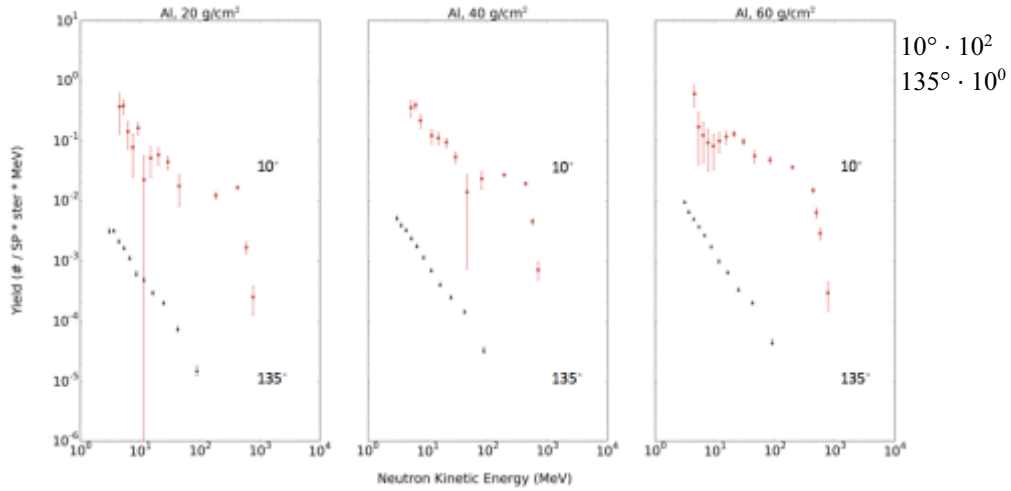

Fig. 6. Background subtracted double differential thick-target neutron yields at 10° and 135° for 400-MeV proton projectiles on 20, 40, and 60 g/cm^2 front and 60 g/cm^2 back aluminum targets. The 10° yields were multiplied by a factor of 100 to prevent overlap.

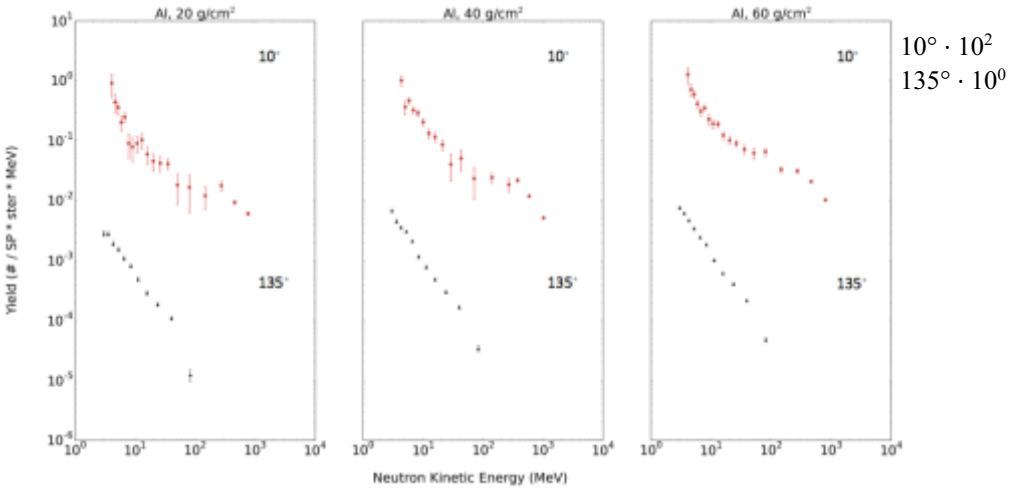

Fig. 7. Background subtracted double differential thick-target neutron yields at 10° and 135° for 800-MeV proton projectiles on 20, 40, and 60 g/cm^2 front and 60 g/cm^2 back aluminum targets. The 10° yields were multiplied by a factor of 100 to prevent overlap.

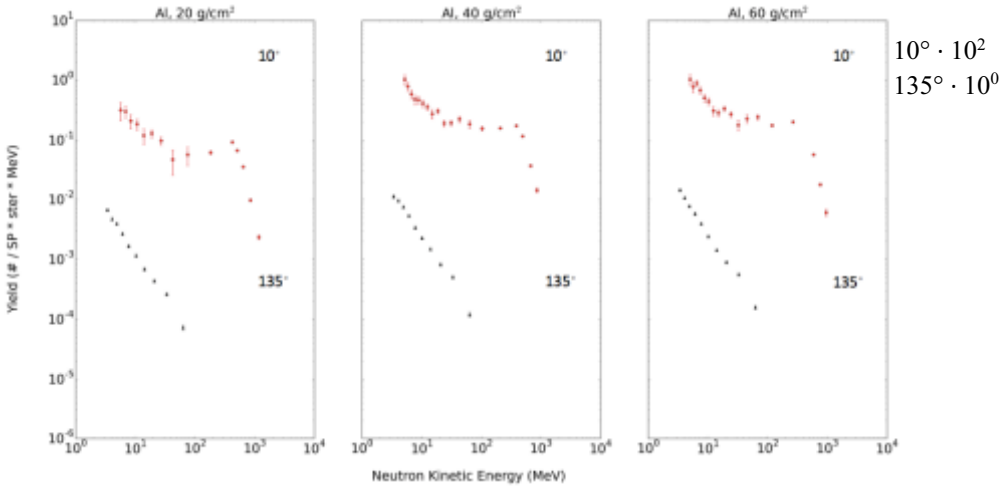

Fig. 8. Background subtracted double differential thick-target neutron yields at 10° and 135° for 400-AMeV helium projectiles on 20, 40, and 60 g/cm^2 front and 60 g/cm^2 back aluminum targets. The 10° yields were multiplied by a factor of 100 to prevent overlap.

5 Future Work

Further analysis will include quantifying the energy resolution of each neutron event using the method described in [9]. ROOT graphical cut uncertainties will be improved by reanalyzing the data with new graphical cuts. A fit to the background data at the 10° liquid scintillator will be considered to improve statistical uncertainties below 100 MeV. Additionally, these experimental results will be compared to MCNP-, PHITS-, and GEANT-simulated double differential thick target yields and their differences will be explored. In addition to this experimental dataset, two 200-hour experiments are scheduled for late 2016 and 2017 at BNL's NSRL. These experiments will follow the same setup and execution of the March 2016 experiment, but will test different beam-target configurations. Targets considered will include 20, 40, and 60 g/cm^2 aluminum and HDPE targets, and ion beams will include proton, helium, carbon, silicon, and iron projectiles at 0.4, 0.8, 1.0, and 2.5 AGeV. The analysis procedure laid out in this paper will be repeated for the new datasets.

6 Summary

100 hours of thick-target experiments were conducted in March 2016 at BNL's NSRL facility. Five ion beam species (400- and 800-AMeV iron, 400 and 800-MeV protons, and 400-AMeV helium) were bombarded on three aluminum upstream targets of varying areal thicknesses (20, 40, or 60 g/cm^2). A second 60 g/cm^2 aluminum target was placed 3.5 m downstream from the front target. Neutrons and light charged ions were measured at six angular locations off beam axis using EJ-301 and EJ-309 liquid scintillators. Neutron events was separated from the gamma and light charged ion events using a series of cuts in ROOT and then normalized to the number of source particles. Data was then background subtracted for each beam-target configuration, and the TDC channels were converted to energy using the time-of-flight method. Finally, neutron yields were corrected for neutron detection efficiency and then normalized to solid angle and energy bin width to produce double differential thick-target yields in units of neutrons / source particle / steradian / MeV. Neutron yields at 10° suffered from a high neutron background due to the liquid scintillator's proximity to the back target, while yields at 135° had the best uncertainties of all the angles. Additional analysis is needed to explore other methods of quantifying background neutrons at 10°, as well as to compare the experimental results presented here to Monte Carlo simulations. Ultimately, the experimental double differential thick target yields will be incorporated into NASA's uncertainty analysis for their radiation transport codes.

This work was supported by Grants NNX12AL51A and NNX15AD89A from the United States National Aeronautics and Space Administration. Special thanks to Matthew Beach, Ph.D. for his assistance with ROOT. Additional thanks to the team at Brookhaven National Laboratory for their extensive assistance with the setup and execution of the experiment.

References

1. P.-E. Tsai, *et. al.*, *2015 IEEE Aerospace Conference*, 1-7 (2015).
2. L. Heilbronn, *et. al.*, Nucl. Sci. Eng., **132**, 1-15 (1999).
3. P.-E. Tsai, "Study of secondary particles produced from heavy-ion interactions," Ph.D. dissertation, Dept. of Nucl. Eng., Univ. of TN, Knoxville, TN (2015).
4. R. Brun, F. Rademakers, Nucl. Instr. Meth. Phys. Res. A, **389**, 81–86 (1997).
5. T. Nakamura, L. Heilbronn, *Handbook on Secondary Particle Production and Transport by High-Energy Heavy Ions* (Singapore: World Scientific Publishing Co. Pte. Ltd., 2006).

6. J. H. Heltsley, *et. al.*, Nucl. Instr. Meth. Phys. Res. A, **263**, 441-445 (1988).
7. V. V. Verbinski, *et. al.*, Nucl. Inst. Meth., **65**, 8–25 (1968).
8. D. Satoh, *et. al.*, J. Nucl. Sci. Tech., **39**, 657–660 (2002).
9. Y. Iwata, *et. al.*, Phys. Rev. C, **64** (2001).